

pubs.acs.org/JACS Article

Dimensionality Engineering of Lead Organic Chalcogenide **Semiconductors**

Hanjun Yang, Sagarmoy Mandal, Yoon Ho Lee, Jee Yung Park, Han Zhao, Chongli Yuan, Libai Huang, Ming Chen,* and Letian Dou*

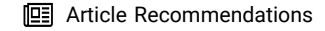


Cite This: J. Am. Chem. Soc. 2023, 145, 23963-23971



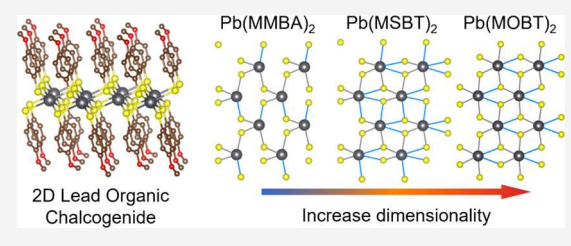
ACCESS I

III Metrics & More



Supporting Information

ABSTRACT: Two-dimensional (2D) metal organic chalcogenides (MOCs) such as silver phenylselenolate (AgSePh) have emerged as a new class of 2D materials due to their unique optical properties. However, these materials typically exhibit large band gaps, and their elemental and structural versatility remain significantly limited. In this work, we synthesize a new family of 2D lead organic chalcogenide (LOC) materials with excellent structural and dimensionality tunability by designing the bonding ability of the organic molecules and the stereochemical activity of the Pb



lone pair. The introduction of electron-donating substituents on the benzenethiol ligands results in a series of LOCs that transition from 1D to 2D, featuring reduced band gaps (down to 1.7 eV), broadband emission, and strong electron-phonon coupling. We demonstrated a prototypical single crystal photodetector with 2D LOC that showed the dimensionality engineering on the transport property of LOC semiconductors. This study paves the way for further development of the synthesis and optical properties of novel organic-inorganic hybrid 2D materials.

INTRODUCTION

Two-dimensional (2D) materials are a class of emerging materials due to their unique optical, electronic, mechanical, and magnetic properties. 1-4 These materials are assembled with monolayers that exhibit strong chemical bonds in-plane but weak van der Waals forces between planes.⁵ Hybrid materials, or materials that involve molecular ligands that guide the bonding of an inorganic motif, have been heavily investigated due to their structural and property-wise versatility.⁶ Among them, coinage metal-based metal organic chalcogenides (MOCs) have received extensive interest, 6-8 especially the 2D silver phenylselenolate (AgSePh) and its derivatives with different organic ligands. $^{9-12}$ This class of 2D materials exhibits strong quantum confinement and tightly bound excitons as multiquantum well systems, 10 leading to intriguing optical properties including blue photoluminescence (PL), fast exciton recombination, 13 in-plane anisotropy, 14 etc. However, so far, the versatility of the coinage metal-based MOCs is limited by the large band gaps (due to the large energy mismatch between the atomic orbitals of silver/copper and sulfur/selenium) and low structural tunability. 15,16 To systematically study the optical properties of MOCs, it is crucial to establish rational principles to design and manipulate their structures and electronic properties.

Lead-based hybrid materials such as 2D lead-halide perovskites have attracted increasing attention in recent years with advantageous properties and versatile applications. 17-23 Their striking optical properties and wide optoelectronic applications are largely attributed to the uniqueness of the 6s

lone pair electrons of Pb2+, which affect both the stereochemistry and the defect tolerance. 24,25 Hence, the success of lead-based hybrid materials inspired us to investigate leadcontaining metal organic chalcogenides or lead organic chalcogenides (LOCs). LOCs feature strong covalent bonds between lead and sulfur while maintaining the structural tunability based on the thiolate group. Prior studies revealed that LOCs tend to form zero-dimensional (0D) and onedimensional (1D) structures, 15,26,27 while the formation of van der Waals 2D structures has been rarely reported.²⁸ The tendency of LOCs forming low-dimensional structures is linked to the prevalence of a hemidirected coordination environment, caused by the statically expressed 6s lone pair, which in turn reduce the coordination number of the Pb-S unit.^{29,30} Therefore, controlling the local stereochemistry is a crucial factor in the design and engineering of the electronic structure of LOCs.

Herein, we report the synthesis of a series of new 2D LOC compounds with high stability and chemically tunable structures. The coordination geometry and bonding modes of LOCs can be engineered by tuning the electron density of the thiol ligands, which is in turn controlled by the substitution

Received: June 1, 2023 Revised: October 10, 2023 Accepted: October 11, 2023

Published: October 28, 2023





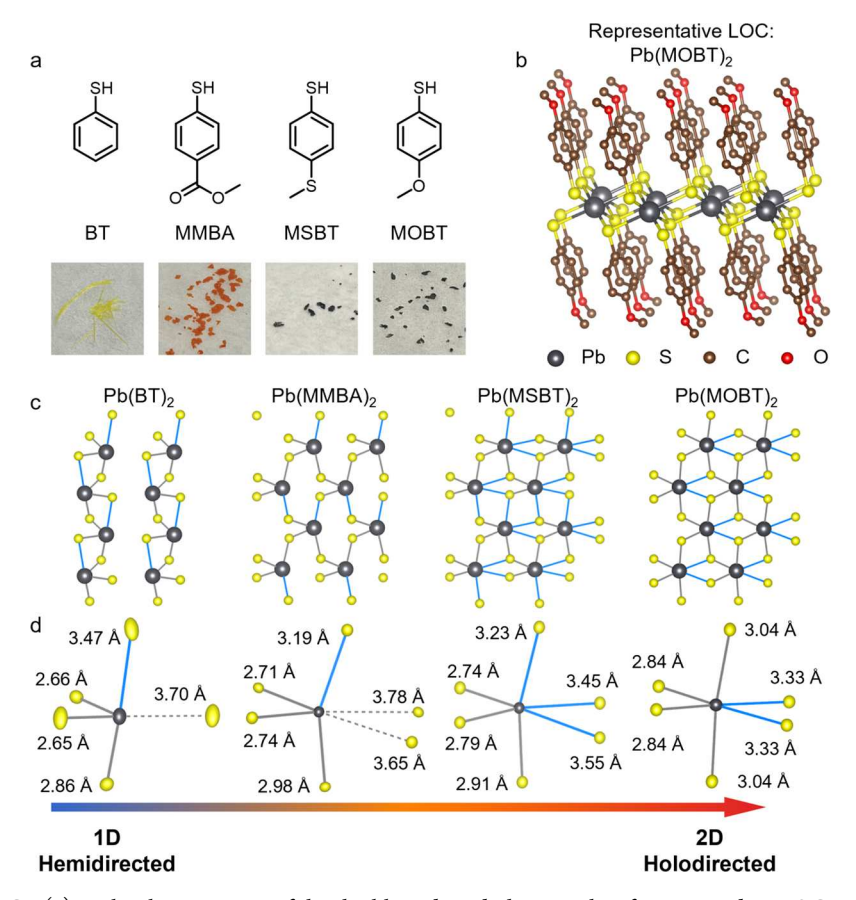


Figure 1. Structures of LOCs. (a) Molecular structures of the thiol ligands and photographs of corresponding LOC single crystals. (b) Schematic illustration of the Pb(MOBT)₂ monolayer. Hydrogen atoms are omitted for clarity. (c) Schematic illustration of the Pb–S network. (d) Local coordination environment of Pb (black) and S (yellow). Short Pb–S bonds (<3.1 Å) are marked in gray color, and long Pb–S bonds (3.1–3.6 Å) are marked in blue. Neighboring nonbonded S atoms (marked in dashed lines) are included for Pb(BT)₂ and Pb(MMBA)₂ to illustrate their structural similarity to Pb(MSBT)₂ and Pb(MOBT)₂.

group in the organic ligand. Molecular design enables continuous tuning of the local coordination from the hemidirected to holodirected coordination sphere. Furthermore, the optical and electronic properties of the LOCs are heavily influenced by the dimensionality. Among 2D LOCs, the band gaps are reduced as the bonding modes evolve from the hemidirected to the holodirected structures. LOCs exhibit broadband self-trapped exciton (STE) emission PL as a result of strong electron—phonon coupling. Prototypical photodetector devices are demonstrated, showing the potential application of LOCs in optoelectronic devices. Our study not only exemplifies a novel family of 2D materials with great structural tunability but also sheds light into the structure—property relationship of lead-based hybrid materials.

RESULTS AND DISCUSSION

Three thiol ligands are mainly investigated in this work, namely, methyl 4-mercaptobenzoate (MMBA), 4-(methylthio)benzenethiol (MSBT), and 4-methoxybenzenethiol (MOBT) (Figure 1a). In addition, the unsubstituted benzenethiol (BT) ligand that forms 1D LOC is also included as the baseline for comparison. 31-33 Some other thiol ligands have also been investigated as potential ligand candidates for 2D LOCs, but due to various factors (such as difficulty in single crystal synthesis, low-dimensional crystal structure, etc.), they were not studied in detail (Figure S1). LOC powders were synthesized by a simple metathesis reaction between lead

acetate and the corresponding thiol ligands. LOC single crystals were then obtained via slow cooling from DMSO/ GBL/ethanol trinary solutions. All LOCs showed lamellar crystal structures, verified by the strong (00n) peaks in their powder XRD profile (Figure S2). The LOC powder showed high stability, with no sign of decomposition, when stored in ambient conditions submerged in water for 6 months (Figure S3). The newly synthesized LOCs showed superior thermal stability to Pb(BT)₂ when annealed at 150 °C overnight, showing no or minimal sign of decomposition, while the XRD of Pb(BT)₂ changed significantly (Figure S4). The elemental stoichiometry of LOC crystals is verified by SEM EDS, showing uniform distribution of Pb and S elements with a ratio of Pb:S $\sim 1:2$ (except for Pb(MSBT)₂ with Pb:S $\sim 1:4$ since each ligand molecule contains two sulfur atoms (Figures S5-S7 and Table S1)).

The crystal structures of the LOCs were resolved by single crystal crystallography. (More information about single crystal crystallography and fitting methods is included in Figures S8–S13 and Tables S2–S5 and following discussion. The crystallographic data of the structures reported in this work have been deposited at the Cambridge Crystallographic Data Centre under deposition numbers 2266800, 2266802, 2266804, and 2291655). Generally, all investigated LOC crystal structures follow a similar scheme, with a layer of PbS₂ unit sandwiched between two layers of organic ligands (Figure 1b, Figures S8–S11, Tables S2–S5). However, the coordina-

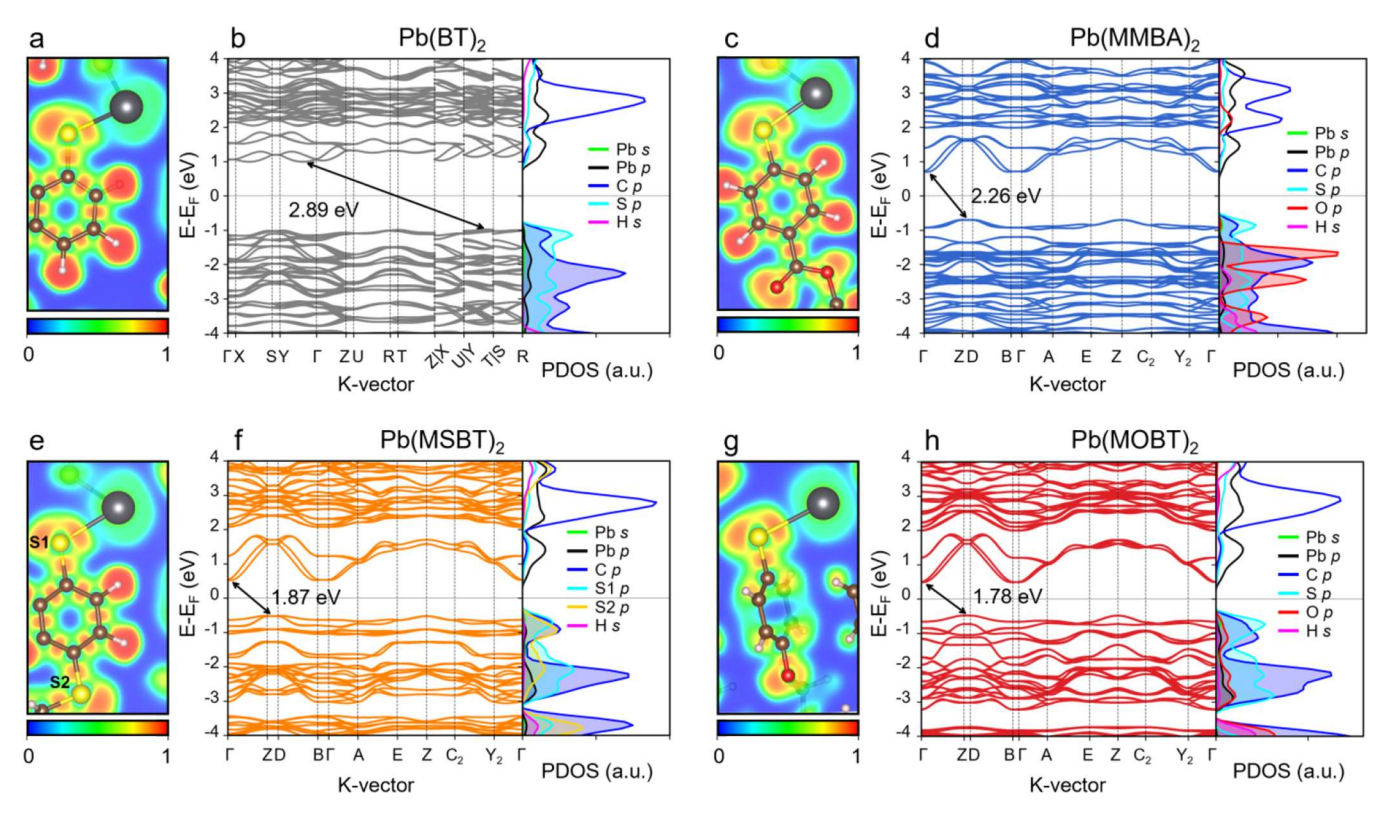


Figure 2. DFT calculations. (a, c, e, g) Calculated electron localization functions of the corresponding compound. Black, yellow, brown, red, and white atoms represent Pb, S, C, O, and H atoms, respectively. (b, d, f, h) Calculated band structure based on the PBE functional and the corresponding projected density of states (PDOS). Valence band maxima and conduction band minima are marked with arrows. The marked band gap values represent the calculated band gap using the HSE06 functional.

tion environment and the connectivity in the LOC structures vary depending on the structure of the organic ligands. The unsubstituted BT ligand results in a heavily hemidirected coordination with 4-coordinated lead connecting into a 1D chain, as reported in previous research (Figure 1c, Figure S8).³¹ On the contrary, substitution on the phenyl ring of the organic ligands results in increased connectivity of the inorganic motif. Specifically, Pb(MMBA)₂ features 4-coordinated lead, organized in 8-member rings with sulfur atoms alternating below and above the basal plane of lead (Figure 1c, Figure S9). Unlike the 1D chain in Pb(BT)₂, the inorganic motif in Pb(MMBA)₂ forms a 2D network, showing increased electronic dimensionality compared with that of the 1D structure of Pb(BT)₂. Considering its lower coordination number in comparison with those of Pb(MSBT)2 and Pb(MOBT)₂ as well as the broken connectivity, it was named a quasi-2D structure. Pb(MSBT)₂ and Pb(MOBT)₂ are both composed of 6-coordinated, edge-sharing PbS₆ octahedra with the facets of the octahedral vertical to the basal plane, resembling the PbI₂ structure (Figure 1c, Figures S10 and S11). In addition to the change in connectivity, the local symmetry of lead is also modulated by the organic structure. Notably, the Pb2+ in both Pb(BT)2 and Pb-(MMBA)₂ possesses hemidirected coordination, evidenced by the asymmetric tetragonal coordination environment where the Pb-S bonds are pushed away from the expressed lone pairs (Figure 1d). In comparison, Pb(MSBT)₂ and Pb(MOBT)₂ exhibit more holodirected coordination modes where the bond angles as well as bond lengths are more uniformly distributed (Table S6).³⁴ It should be noted that the transition from Pb(MMBA)₂ to Pb(MOBT)₂ is a gradual shift in bond lengths

and angles, rather than a complete reconfiguration from Pb(BT)₂ to Pb(MMBA)₂. The positions of the two nonbonded neighboring sulfur atoms in Pb(MMBA)₂ resemble two of the bonded sulfur atoms in Pb(MSBT)2 or Pb-(MOBT)₂. On the other hand, the structure of the inorganic motif of Pb(BT)₂ is largely unsimilar to the other three LOCs (Figure 1c,d). 4-Mercaptophenol (MP), featuring a hydroxyl group instead of the methoxy group in MOBT, was found to form Pb(MP)2 with an interlayer hydrogen bond and showed very similar crystal structure and optical properties to Pb(MOBT)₂ (Figures S12-S14). All aspects considered, by designing the organic ligand structures of the LOC compounds, their electronic dimensionality can be continuously tuned from 1D to 2D, and their coordination symmetry can be gradually modulated from hemidirected to holodirected environments.

The crystal structures of LOCs are composed of individual 2D layers that are vertically separated by organic ligands, which are connected by weak van der Waals interactions between organic molecules. Therefore, we present a facile mechanical exfoliation method with Scotch tape to obtain 2D nanocrystals of LOCs (Figure S15). The exfoliated crystals exhibit a thickness below 100 nm, showing that the weak van der Waals interaction between layers can be easily broken. Fluorescence lifetime imaging microscopy (FLIM) confirmed that the exfoliated LOC samples showed uniform PL intensity and lifetimes (Figure S16) without significant edge effects. The uniformity of PL emission demonstrated the stability and uniformity of the LOC nanocrystals obtained by mechanical exfoliation. On the contrary, Pb(MP)₂, which features interlayer hydrogen bonds, cannot be exfoliated to nanocryst-

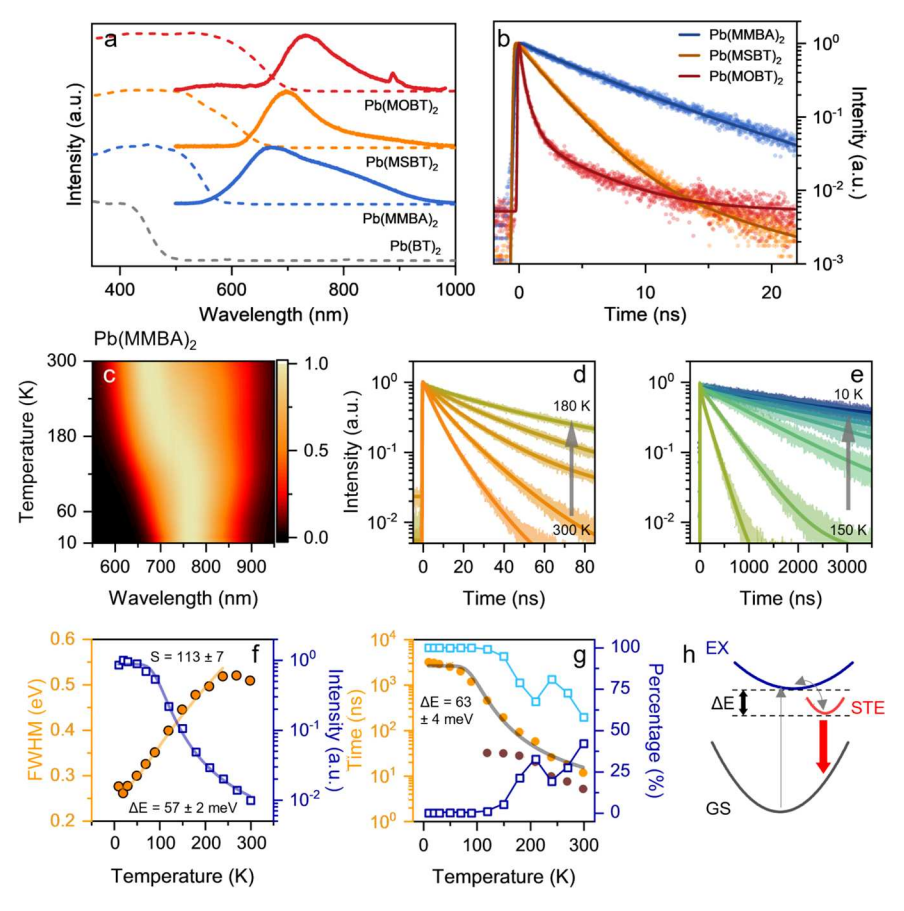


Figure 3. (a) Absorption (dashed lines) and PL (solid lines) spectra of the LOC samples. Absorption spectra were based on powder diffuse reflectance spectra using Kubelka—Munk transformation. PL spectra were measured on exfoliated crystals. (b) TRPL spectra of exfoliated LOC samples. (c) Normalized temperature-dependent PL spectra of Pb(MMBA)₂. (d, e) Temperature-dependent TRPL spectra of Pb(MMBA)₂. (f) Evolution of the PL full-width at half-maximum (fwhm, orange circles) and PL intensity (blue squares) as a function of temperature. (g) Evolution of the TRPL lifetimes (solid circles) and the corresponding percentages (open squares) based on biexponential fitting. Bright symbols represent the long lifetime component, and dark symbols represent the short lifetime component. (h) Schematic illustration of the STE PL mechanism. GS: ground state; EX: excited state; ΔE: trapping energy.

als. Overall, we confirmed that mechanical exfoliation is a valid method to produce LOC thin nanocrystals with comparable quality to the original single crystal.

Density functional theory (DFT) calculations were performed to understand the structural and electronic properties of the LOC compounds. The calculation-optimized structure showed a negligible difference from experimental results (Figure S17, Table S7). The evolution of the lead coordination environment from hemidirected to holodirected is clearly illustrated by the electron localization function (ELF) diagrams (Figure 2a,c,e,g).35 The lead atoms in Pb(BT)2 exhibit stereochemically active lone pairs, as shown in the asymmetric electron localization around the lead atom. The electron localization function of Pb2+ becomes gradually more symmetric from hemidirected Pb(BT)₂ and Pb(MMBA)₂ to holodirected Pb(MSBT)₂ and Pb(MOBT)₂. In addition, Löwdin charge analysis shows that the average partial charge over the S atoms of the thiol groups decreases from -0.0898, -0.0932, -0.103 to -0.113 for Pb(BT)₂, Pb(MMBA)₂, Pb(MSBT)₂, and Pb(MOBT)₂, respectively. As a result of the increased electron density and thus stronger affinity to Pb²⁺, the coordination numbers of sulfur increase from 2coordinated in Pb(BT)₂ and Pb(MMBA)₂ to 3-coordinated in Pb(MSBT)₂ and Pb(MOBT)₂. Correspondingly, the charge density around Pb atoms increased from +0.4789 for Pb(BT)₂ to +0.5001, +0.5017, and +0.5123 for Pb(MMBA)₂, Pb-(MSBT)₂, and Pb(MOBT)₂. The increased positive charge contributes to the reduced spatial hindrance of the 6s lone pair and thus the transition from hemidirected to holodirected modes.³⁰ It is clear that the molecule's increased electron density on the thiol ligands contributes to both the transition to a holodirected coordination sphere and increased coordination number.

DFT calculations show indirect band gaps of 2.89, 2.26, 1.87, and 1.78 eV for Pb(BT)₂, Pb(MMBA)₂, Pb(MSBT)₂, and Pb(MOBT)₂, respectively (Figure 2b,d,f,h). The decreasing trend of the band gaps reflects an increase in the electronic dimensionality from the 1D Pb(BT)₂ to the quasi-2D Pb(MMBA)₂ with a low coordination number and then to the 2D Pb(MSBT)₂ and Pb(MOBT)₂, which feature a 2D structure with PbS₆ octahedral. The projected density of states (PDOS) reveals that for all LOCs, valence band maxima (VBMs) are mainly associated with the p orbitals of C and S atoms from the organic ligands, while the conduction band minima (CBMs) mainly arise from the p orbitals of Pb. Therefore, in addition to the increased dimensionality change, the electron-donating substitution groups on the organic ligands and thus the raised energy level of the organic ligands is another factor toward the decreased band gap. The VBM and CBM bands of the 2D LOCs are significantly more dispersive

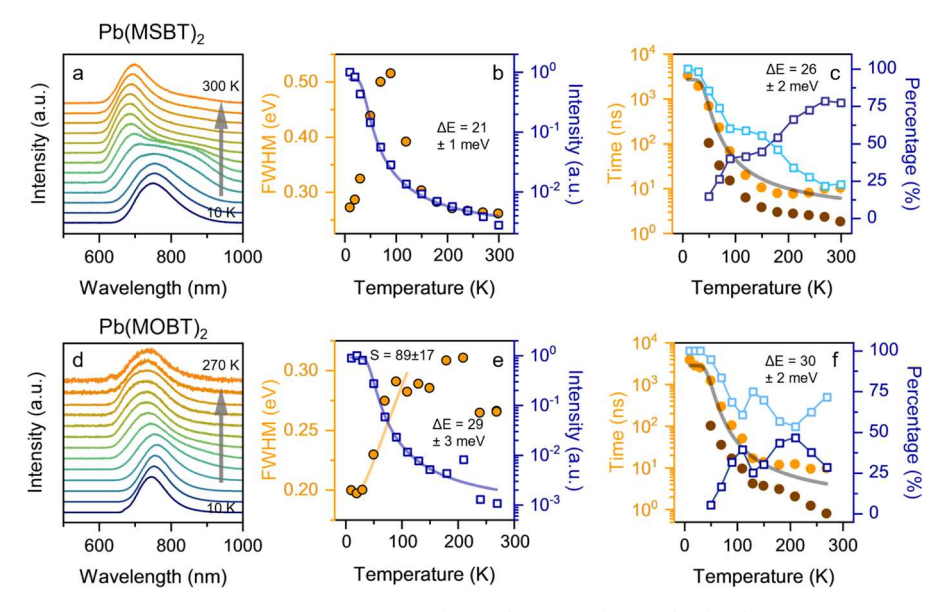


Figure 4. (a, d) Normalized temperature-dependent PL spectra of Pb(MSBT)₂ and Pb(MOBT)₂. (b, e) Evolution of the PL fwhm (orange circles) and PL intensity (blue squares) as a function of temperature. (c, f) Evolution of the TRPL lifetimes (solid circles) and the corresponding percentages (open squares) based on biexponential fitting.

than those of 1D Pb(BT)₂, suggesting reduced effective mass and enhanced transport properties. Overall, the band structures of the LOC compounds can be fine-tuned by adjusting the structures of the organic ligands, showing enhanced tunability than some other 2D hybrid materials such as Ruddlesden—Popper phase 2D perovskites, where the organic ligands have no covalent bond to the inorganic motif.

Experimentally, Pb(BT)₂, Pb(MMBA)₂, Pb(MSBT)₂, and Pb(MOBT)₂ exhibit optical band gaps of 2.46, 2.10, 1.80, and 1.69 eV, respectively, based on diffuse reflectance measurement (Figure 3a, Figure S18). The observed decreasing trend of band gaps is very consistent with the DFT calculations (Table S8). Absorption spectra based on thin film samples showed a rather broad absorption profile, corresponding to the indirect band gap of LOCs (Figure S19). Both diffuse reflectance and thin film absorption spectra confirmed the indirect band gap. All LOCs (except for Pb(BT), where no PL is observed at room temperature) exhibit broad PL emission with a large Stokes shift from their absorption edges. Specifically, Pb(MMBA)₂ exhibited a broad PL profile composed of a 675 nm peak and a broad tail around 770 nm, while Pb(MSBT)₂ and Pb(MOBT)₂ showed relatively symmetric PL peaks at 707 and 738 nm, respectively. The PL intensity follows the general trend of Pb(MMBA)₂ > Pb(MSBT)₂ > Pb(MOBT)₂, although the absolute PL quantum yields (QYs) were not quantified due to the weak PL intensity (estimated PLQY < 1% for all LOCs). The low PLQYs are likely a result of the indirect band gaps. The timeresolved photoluminescence (TRPL) spectra of all three LOC compounds exhibit lifetime in the nanosecond range, between 8.7 and 1.7 ns (Figure 3b, Table S9). LOCs showed a linear power dependence in the PL properties, indicating that nonlinear recombination processes are insignificant in the LOCs under the excitation power used in this study (Figure S20)

Temperature-dependent PL and TRPL were carried out to understand exciton dynamics and electron—phonon interactions. For Pb(MMBA)₂, the PL peak centered at 675 nm gradually decreases relative to the low energy tail as the

temperature decreases, and the PL peak is centered at ~770 nm below 90 K (Figure 3c, Figure S21). Furthermore, the temperature-dependent TRPL shifts from the biexponential decay to monoexponential decay with lower temperatures, accompanied by a significant increase in average PL lifetime from ~10 ns to >1000 ns at 10 K (Figure 3d,e). We note that the PL lifetime of Pb(MMBA)₂ exhibits around two orders of magnitude change from room temperature to 80 K, showing potential remote thermometry application.³⁶ Assuming that the electron—phonon coupling is the main broadening mechanism for PL peaks in the low-temperature range, then the full-width at half-maximum (fwhm) of temperature-dependent PL can be fitted using the following expression:^{37,38}

$$fwhm = 2.36\sqrt{S}E_{ph}\sqrt{\coth\frac{E_{ph}}{2k_{B}T}}$$
(1)

where *S* represents the Huang–Rhys factor and $E_{\rm ph}$ represents the phonon energy (Figure 3f). A large *S* of 113 \pm 7 and a phonon energy of 10.8 \pm 0.5 meV are obtained, reflecting large electron–phonon coupling in the LOC sample.³⁹

The strong coupling between excitons and phonons at the excited state could result in considerable configuration deformation and the formation of STEs. The STE emission in LOC samples is further supported by the characteristic linear power dependence, broad PL profile at low temperatures, and monoexponential TRPL decay. The trapping energy, which shows the extent of lattice deformation as a result of exciton self-trapping, is crucial to understanding the STE PL properties. Assuming that the lifetime (slow component) change over temperature is governed by the thermal distribution between the trapped and free states, a trapping energy of 63 ± 4 meV is derived by the temperature-dependent TRPL spectra using the following eq (Figure 3g) the spectra using the following eq (Figure 3g) the second state of the exciton section of the second se

$$t = \frac{t_0}{1 + Ae^{-\Delta E/k_{\rm B}T}} \tag{2}$$

where t_0 represents the radiative lifetime of STE at 0 K, ΔE represents the trapping energy, and A is a constant. The low

trapping energy, which is smaller than those of low-dimensional luminescent materials that are based on the STE mechanism, $^{41,43-45}$ results in rapid detrapping at ambient temperature and thus low PL efficiency, asymmetric PL profile, and biexpotential TRPL traces (Figure 3h). On the contrary, at low temperatures where thermal distribution is negligible, the emission behavior is more representative of the STE mechanism. A similar trapping energy of 57 ± 2 meV can be obtained by a similar fitting based on temperature-dependent PL intensity, verifying the validity of trapping energy based on TRPL fitting. 46

The other LOCs exhibit similar PL properties within the STE model. Pb(BT)₂ exhibits a broad weak PL centered at 820 nm at 10 K, quickly weakened upon raising the temperature until it became negligible at >140 K (Figure S22). For Pb(MSBT)₂ and Pb(MOBT)₂, the PL intensity also significantly increases as the temperature decreases (Figure 4). The PL line width of both Pb(MSBT)₂ and Pb(MOBT)₂ exhibits a giant broadening starting around 90 K (Figure 4a). We tentatively assume that while the STE is prominent at low temperatures for these two compounds, near room temperature, the free exciton emission coexists with STE emission due to low trapping energies. Strong electron-phonon coupling is observed in both compounds, as is shown by the broad PL profile and the large Huang-Rhys factor (S = 89 for Pb(MOBT)₂ based on the PL broadening at low temperature). Quantitively, based on the temperature-dependent TRPL, trapping energies of 26 and 30 meV are obtained for Pb(MSBT)₂ and Pb(MOBT), respectively (Figure 4c,f and Figures S23 and S24). The low trapping energy of Pb(MSBT)₂ and Pb(MOBT)₂ compared with Pb(MMBA)₂ is consistent with their lower PL efficiencies at ambient temperature. A larger trapping energy is typically associated with a higher degree of structural deformation,⁴⁷ which is prominent for Pb(MMBA)₂ considering its hemidirected coordination environment. Therefore, it should be expected that increasing the deformation via molecular design while maintaining the 2D structure of LOC would further improve its emission efficiency. In addition, the indirect band gaps of LOCs likely caused the prevalence of STE emission over the band edge emission. For example, in terms of the Ag-based MOCs, the PL of AgSePh, which exhibits a direct band gap, is dominated by the free excitons, while a recent report on AgTePh, which has an indirect band gap, was characterized as a barrier-less STE emission with a trapping energy around 50 meV.⁴⁸

Furthermore, we demonstrated the viability of LOCs in optoelectronic devices by the fabrication of a prototypical single crystal photodetector. Exfoliated single crystals were drytransferred to prepatterned gold electrodes with a gap of 3 μ m (Figure 5a,c). Both of the 1D Pb(BT)₂ and the 2D Pb(MOBT)₂ showed low current in the dark, likely limited by their very low intrinsic carrier concentration or nonideal contact (Figure 5b,d). However, while the Pb(BT)₂ device showed almost no photoresponse under UV illumination, the current density of the Pb(MOBT)₂ device showed an enhancement of ~100 times at a light intensity of 25 mW/cm². The stark difference suggests that the 2D LOC provides a carrier mobility higher than that of the 1D counterpart. These preliminary results suggest that 2D LOCs are promising candidates for applications in optoelectronic devices.

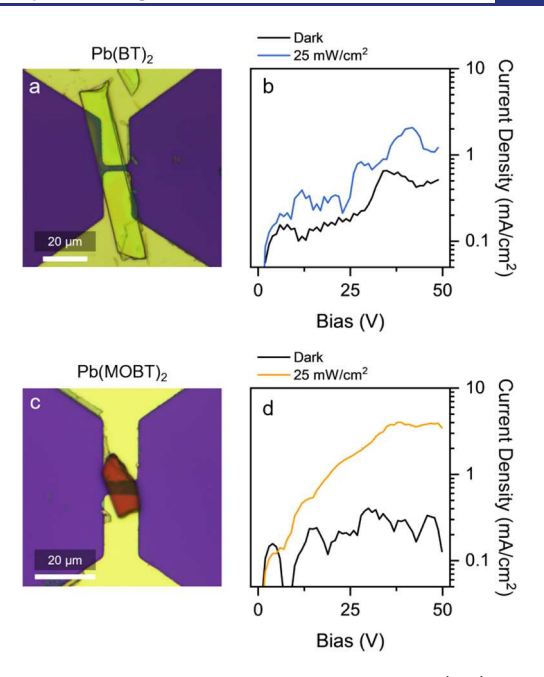


Figure 5. Photoconductivity measurements of $Pb(BT)_2$ and $Pb(MOBT)_2$. (a, c) Measurement setup. (b, d) Current density of $Pb(BT)_2$ and $Pb(MOBT)_2$ single crystals in the dark and under illumination.

CONCLUSIONS

In summary, we report the synthesis of three new 2D LOC compounds. The local bonding coordination environment can be systematically tuned from hemidirected to holodirected by increasing the electron density of thiol. In addition, the electron dimensionality and therefore the band gaps of the LOC materials can be manipulated by ligand design. The LOCs exhibit large electron—phonon coupling and broadband self-trapped exciton emission with a low trapping energy. We demonstrated a prototypical photodetector based on the holodirected 2D Pb(MOBT)₂ single crystal. The engineering of thiol ligands can serve as a blueprint for the further design of the MOC to expand the structural and property library of the emerging family of hybrid 2D materials.

METHODS

Synthesis of Lead-Organic Chalcogenides. MMBA was purchased from Combi-Block. All other chemicals were purchased from Sigma-Aldrich. All chemicals were used as received. The powders of LOCs were synthesized by a facile metathesis reaction. Briefly, 1.2 mmol of lead acetate trihydrate (Pb(OAc)2·3H2O) was dissolved in 5 mL of methanol at 55 °C. Then, 2.5 mmol of the respective thiol ligand was dissolved in 2 mL of methanol and then slowly added to the lead acetate solution under vigorous stirring. The mixture was then allowed to react for 2 h at 55 °C. The powder products were collected by filtration and dried under vacuum. The single crystals were recrystallized from powder samples by a slowcooling method from the mixed solution of γ -butyrolactone (GBL), dimethyl sulfoxide (DMSO), and ethanol (EtOH). Ten milligrams of Pb(MMBA), powder was dissolved in 200 μ L of GBL, 50 μ L of DMSO, and 50 μ L of EtOH; 10 mg of Pb(MSBT)₂ powder was dissolved in 400 μ L of GBL, 200 μ L of DMSO, and 80 μ L of EtOH; 10 mg of Pb(MOBT)₂ powder was dissolved in 400 μ L of GBL, 100 μ L of DMSO, and 120 μ L of EtOH; 10 mg of Pb(BT)₂ powder was dissolved in 400 μ L of GBL, 200 μ L of DMSO, and 700 μ L of EtOH. The solutions were allowed to cool down from 100 °C to room temperature in 3 days. The single crystals formed were then collected by filtration. Pb(MP)₂ single were obtained by a solvent diffusion

method. A total of 10 mg of Pb(MP)₂ powder was dissolved in 200 μL of DMSO in a 4 mL vial, and water vapor was allowed to diffuse into the vial at room temperature until a black crystal formed.

Optical Characterization. Diffuse reflectance spectra were measured on a PerkinElmer Lambda950 UV-vis-NIR spectrophotometer based on powder samples. Absorption spectra were measured on an Agilent Technologies Cary 60 UV-vis Spectrometer in transmission mode. The absorption samples were prepared by spincoating the 0.1 M 1:1 GBL:DMSO solution of LOC powders. A total of 30 μ L of the stock solution was spin-coated on glass slides at 3000 rpm and annealed at 120 °C for 10 min. The single crystals were mechanically exfoliated with Scotch brand tape for other optical characterizations. Optical images were measured by a custom Olympus BX53 microscope. Dark field images were excited by a UV light source (012-63000; X-CITE 120 REPL LAMP) with a 330-385 nm band-pass filter or a Coherent OBIS 375 nm laser. PL and TRPL spectra were measured by a home-built PL microscope. A femtosecond pulsed laser (Light conversion, Orpheus high power optical parametric amplifier, ORPHEUS-HP; carbide femtosecond laser system, CB3-40W) with an excitation wavelength of 447 nm and 2.03 MHz-203 kHz repetition rate was used as excitation, focused with a 40× objective with a numerical aperture (NA) of 0.6. The PL emission was collected with the same objective, dispersed with a monochromator (Andor Technology), and detected by a thermoelectric cooled charge coupled detector (Andor Technology). TRPL was measured by a single-photon avalanche diode and a singlephoton counting module (PicoQuant) with a time resolution of 16-64 ps. TRPL traces were fitted with biexponential or triexponential decay convoluted with instrumental response function as below:

$$I(t) = \operatorname{conv}\left(\exp\left(-\frac{t^2}{w^2}\right), \Theta(t_0) \cdot \sum_{n} \left(A_n \cdot \exp\left(-\frac{t}{\tau_n}\right)\right)\right)$$

Temperature-dependent PL and TRPL were measured by a homebuilt PL microscope coupled with a Montana s50 cryostation with the same excitation source and detector.

Structural Characterizations. Powder XRD was measured by a Panalytical Empyrean Powder X-ray Diffractometer with a Cu K α source. SEM data were collected on a Hitachi cold SEM S-4800 model. AFM was collected in tapping mode on a Nixon System NX10 atomic force microscope. Single crystal crystallography collection methods are summarized in the Supporting Information.

Device Fabrication. The Ti/Au electrodes were prepared by conventional photolithography and a thermal evaporation method on Si/SiO₂ substrates. After the patterning process of photoresist, Ti(5 nm)/Au (130 nm) was thermally evaporated onto the substrate followed by acetone washing to remove the photoresist. Subsequently, exfoliated crystals were transferred on the electrodes via a dry transfer method using PDMS stamps. The current-voltage characteristics of the crystals were measured using a Keithley 4200-SCS semiconductor parametric analyzer. A hand-held UV lamp at 365 nm was used as the

Calculation Methods. To support the experimental results, the structural and electronic properties of all of the LOCs were calculated using density functional theory (DFT). All the calculations were performed within the framework of periodic DFT employing the Quantum ESPRESSO package. 49 The Perdew-Burke-Ernzerhof (PBE)⁵⁰ functional at the level of generalized gradient approximation (GGA) was used together with projector augmented wave (PAW)⁵¹ type pseudopotentials. To account for van der Waals (VdW) interactions, the calculations were performed including Grimme's D3 correction. 52 The wave functions and electron densities were expanded in a plane wave (PW) basis set with cutoffs of 80 and 400 Ry, respectively. The wave functions were converged when the magnitude of change in energy is below 10^{-8} Ry. The convergence criteria for the optimization of lattice parameters and the geometries were set to 0.5 kbar and 10⁻⁴ Ry/au, respectively. The Brillouin zone was sampled with Γ -centered k-point mesh of $1 \times 6 \times 6$ for the Pb(BT)₂ system. For Pb(MMBA)₂, Pb(MSBT)₂, and Pb(MOBT)₂ systems, a Γ -centered k-point mesh of 6 \times 6 \times 1 was used.

Additionally, for accurate estimation of band gaps, the Heyd-Scuseria-Ernzerhof (HSE06)⁵³ hybrid functional was used together with norm-conserving-type pseudopotentials. In these calculations, PW cutoffs of 60 and 300 Ry were used for expanding the wave functions and the densities, respectively. Band gap calculation of the Pb(BT)₂ system was performed with a Γ -centered k-point mesh of 1 \times 4 \times 4, whereas, for Pb(MMBA)₂, Pb(MSBT)₂, and Pb(MOBT)₂ systems, a Γ -centered k-point mesh of 4 \times 4 \times 1 was used. To incorporate the relativistic effect of Pb atoms, spin-orbit coupling was included during the band structure calculations with PBE and HSE06 functionals.

ASSOCIATED CONTENT

Supporting Information

The Supporting Information is available free of charge at https://pubs.acs.org/doi/10.1021/jacs.3c05745.

XRD, SEM, crystal structure illustrations, additional crystallographic data, diffuse reflectance spectra, FLIM images, additional PL spectra and TRPL spectra (PDF)

Accession Codes

CCDC 2266800, 2266802, 2266804, and 2291655 contain the supplementary crystallographic data for this paper. These data can be obtained free of charge via www.ccdc.cam.ac.uk/ data request/cif, or by emailing data request@ccdc.cam.ac. uk, or by contacting The Cambridge Crystallographic Data Centre, 12 Union Road, Cambridge CB2 1EZ, UK; fax: +44 1223 336033.

AUTHOR INFORMATION

Corresponding Authors

Ming Chen – Department of Chemistry, Purdue University, West Lafayette, Indiana 47907, United States; o orcid.org/ 0000-0001-6205-7107; Email: chen4116@purdue.edu

Letian Dou - Department of Chemistry and Davidson School of Chemical Engineering, Purdue University, West Lafayette, Indiana 47907, United States; orcid.org/0000-0001-6411-8591; Email: dou10@purdue.edu

Authors

Hanjun Yang - Davidson School of Chemical Engineering and Department of Chemistry, Purdue University, West Lafayette, Indiana 47907, United States; o orcid.org/0000-0002-6856-6559

Sagarmoy Mandal – Department of Chemistry, Purdue University, West Lafayette, Indiana 47907, United States; orcid.org/0000-0002-4674-6583

Yoon Ho Lee – Davidson School of Chemical Engineering and Department of Chemistry, Purdue University, West Lafayette, Indiana 47907, United States

Jee Yung Park - Davidson School of Chemical Engineering, Purdue University, West Lafayette, Indiana 47907, United States; o orcid.org/0000-0002-9814-6563

Han Zhao - Davidson School of Chemical Engineering, Purdue University, West Lafayette, Indiana 47907, United

Chongli Yuan - Davidson School of Chemical Engineering, Purdue University, West Lafayette, Indiana 47907, United States; orcid.org/0000-0003-3765-0931

Libai Huang – Department of Chemistry, Purdue University, West Lafayette, Indiana 47907, United States; o orcid.org/ 0000-0001-9975-3624

Complete contact information is available at: https://pubs.acs.org/10.1021/jacs.3c05745

Notes

The authors declare no competing financial interest.

ACKNOWLEDGMENTS

This work is primarily supported by the US Department of Energy, Office of Basic Energy Sciences under award number DE-SC0022082. H.Y. acknowledges financial support from the Lillian Gilbreth Postdoc Fellowship by the college of engineering of Purdue University. S.M. and M.C. gratefully acknowledge financial support from the National Science Foundation (EAR-2246687). Computational resources were provided by the National Energy Research Scientific Computing Center (NERSC), a U.S. Department of Energy Office of Science User Facility, operated under Contract No. DE-AC02-05CH11231 and the Extreme Science and Engineering Discovery Environment (XSEDE), which is supported by the National Science Foundation grant number ACI-1548562. Authors thank Matthias Zeller from Department of Chemistry, Purdue University for the measurement of single crystals and valuable discussions.

REFERENCES

- (1) Novoselov, K. S.; Geim, A. K.; Morozov, S. V.; Jiang, D.; Zhang, Y.; Dubonos, S. V.; Grigorieva, I. V.; Firsov, A. A. Electric Field Effect in Atomically Thin Carbon Films. *Science* **2004**, *306* (5696), 666–669.
- (2) Lin, H.; Zhang, Z.; Zhang, H.; Lin, K.-T.; Wen, X.; Liang, Y.; Fu, Y.; Lau, A. K. T.; Ma, T.; Qiu, C.-W.; et al. Engineering van der Waals Materials for Advanced Metaphotonics. *Chem. Rev.* **2022**, *122* (19), 15204–15355.
- (3) Mak, K. F.; Lee, C.; Hone, J.; Shan, J.; Heinz, T. F. Atomically Thin MoS_2 : A New Direct-Gap Semiconductor. *Phys. Rev. Lett.* **2010**, 105 (13), No. 136805.
- (4) Tan, C.; Cao, X.; Wu, X.-J.; He, Q.; Yang, J.; Zhang, X.; Chen, J.; Zhao, W.; Han, S.; Nam, G.-H.; et al. Recent Advances in Ultrathin Two-Dimensional Nanomaterials. *Chem. Rev.* **2017**, *117* (9), 6225–6331.
- (5) Novoselov, K. S.; Mishchenko, A.; Carvalho, A.; Castro Neto, A. H. 2D materials and van der Waals heterostructures. *Science* **2016**, 353 (6298), aac9439.
- (6) Yan, H.; Hohman, J. N.; Li, F. H.; Jia, C.; Solis-Ibarra, D.; Wu, B.; Dahl, J. E. P.; Carlson, R. M. K.; Tkachenko, B. A.; Fokin, A. A.; et al. Hybrid metal—organic chalcogenide nanowires with electrically conductive inorganic core through diamondoid-directed assembly. *Nat. Mater.* **2017**, *16* (3), 349–355.
- (7) Li, Y.; Jiang, X.; Fu, Z.; Huang, Q.; Wang, G.-E.; Deng, W.-H.; Wang, C.; Li, Z.; Yin, W.; Chen, B.; et al. Coordination assembly of 2D ordered organic metal chalcogenides with widely tunable electronic band gaps. *Nat. Commun.* **2020**, *11* (1), 261.
- (8) Veselska, O.; Demessence, A. d¹⁰ coinage metal organic chalcogenolates: From oligomers to coordination polymers. *Coord. Chem. Rev.* **2018**, 355, 240–270.
- (9) Schriber, E. A.; Popple, D. C.; Yeung, M.; Brady, M. A.; Corlett, S. A.; Hohman, J. N. Mithrene Is a Self-Assembling Robustly Blue Luminescent Metal—Organic Chalcogenolate Assembly for 2D Optoelectronic Applications. ACS Appl. Nano Mater. 2018, 1 (7), 3498—3508.
- (10) Yao, K.; Collins, M. S.; Nell, K. M.; Barnard, E. S.; Borys, N. J.; Kuykendall, T.; Hohman, J. N.; Schuck, P. J. Strongly Quantum-Confined Blue-Emitting Excitons in Chemically Configurable Multiquantum Wells. *ACS Nano* **2021**, *15* (3), 4085–4092.
- (11) Paritmongkol, W.; Sakurada, T.; Lee, W. S.; Wan, R.; Müller, P.; Tisdale, W. A. Size and Quality Enhancement of 2D Semiconducting Metal—Organic Chalcogenolates by Amine Addition. *J. Am. Chem. Soc.* **2021**, *143* (48), 20256–20263.

- (12) Trang, B.; Yeung, M.; Popple, D. C.; Schriber, E. A.; Brady, M. A.; Kuykendall, T. R.; Hohman, J. N. Tarnishing Silver Metal into Mithrene. J. Am. Chem. Soc. 2018, 140 (42), 13892–13903.
- (13) Kastl, C.; Schwartzberg, A. M.; Maserati, L. Picoseconds-Limited Exciton Recombination in Metal—Organic Chalcogenides Hybrid Quantum Wells. *ACS Nano* **2022**, *16* (3), 3715–3722.
- (14) Maserati, L.; Refaely-Abramson, S.; Kastl, C.; Chen, C. T.; Borys, N. J.; Eisler, C. N.; Collins, M. S.; Smidt, T. E.; Barnard, E. S.; Strasbourg, M.; et al. Anisotropic 2D excitons unveiled in organic—inorganic quantum wells. *Mater. Horiz.* **2021**, 8 (1), 197–208.
- (15) Yeung, M.; Popple, D. C.; Schriber, E. A.; Teat, S. J.; Beavers, C. M.; Demessence, A.; Kuykendall, T. R.; Hohman, J. N. Corrosion of Late- and Post-Transition Metals into Metal—Organic Chalcogenolates and Implications for Nanodevice Architectures. ACS Appl. Nano Mater. 2020, 3 (4), 3568—3577.
- (16) Sakurada, T.; Cho, Y.; Paritmongkol, W.; Lee, W. S.; Wan, R.; Su, A.; Shcherbakov-Wu, W.; Müller, P.; Kulik, H. J.; Tisdale, W. A. 1D Hybrid Semiconductor Silver 2,6-Difluorophenylselenolate. *J. Am. Chem. Soc.* **2023**, *145* (9), 5183–5190.
- (17) Stoumpos, C. C.; Cao, D. H.; Clark, D. J.; Young, J.; Rondinelli, J. M.; Jang, J. I.; Hupp, J. T.; Kanatzidis, M. G. Ruddlesden–Popper Hybrid Lead Iodide Perovskite 2D Homologous Semiconductors. *Chem. Mater.* **2016**, 28 (8), 2852–2867.
- (18) Li, X.; Hoffman, J. M.; Kanatzidis, M. G. The 2D Halide Perovskite Rulebook: How the Spacer Influences Everything from the Structure to Optoelectronic Device Efficiency. *Chem. Rev.* **2021**, *121* (4), 2230–2291.
- (19) Shi, E.; Gao, Y.; Finkenauer, B. P.; Akriti; Coffey, A. H.; Dou, L. Two-dimensional halide perovskite nanomaterials and heterostructures. *Chem. Soc. Rev.* **2018**, 47 (16), 6046–6072.
- (20) Ren, H.; Yu, S.; Chao, L.; Xia, Y.; Sun, Y.; Zuo, S.; Li, F.; Niu, T.; Yang, Y.; Ju, H.; et al. Efficient and stable Ruddlesden–Popper perovskite solar cell with tailored interlayer molecular interaction. *Nat. Photonics* **2020**, *14* (3), 154–163.
- (21) Brivio, F.; Butler, K. T.; Walsh, A.; van Schilfgaarde, M. Relativistic quasiparticle self-consistent electronic structure of hybrid halide perovskite photovoltaic absorbers. *Phys. Rev. B* **2014**, *89* (15), No. 155204.
- (22) Wang, K.; Jin, L.; Gao, Y.; Liang, A.; Finkenauer, B. P.; Zhao, W.; Wei, Z.; Zhu, C.; Guo, T.-F.; Huang, L.; et al. Lead-Free Organic-Perovskite Hybrid Quantum Wells for Highly Stable Light-Emitting Diodes. ACS Nano 2021, 15 (4), 6316–6325.
- (23) Tsai, H.; Nie, W.; Blancon, J.-C.; Stoumpos, C. C.; Asadpour, R.; Harutyunyan, B.; Neukirch, A. J.; Verduzco, R.; Crochet, J. J.; Tretiak, S.; et al. High-efficiency two-dimensional Ruddlesden—Popper perovskite solar cells. *Nature* **2016**, *536* (7616), 312—316.
- (24) McCall, K. M.; Morad, V.; Benin, B. M.; Kovalenko, M. V. Efficient Lone-Pair-Driven Luminescence: Structure—Property Relationships in Emissive 5s² Metal Halides. *ACS Mater. Lett.* **2020**, 2 (9), 1218–1232.
- (25) Li, T.; Luo, S.; Wang, X.; Zhang, L. Alternative Lone-Pair ns²-Cation-Based Semiconductors beyond Lead Halide Perovskites for Optoelectronic Applications. *Adv. Mater.* **2021**, *33* (32), 2008574.
- (26) Imran, M.; Mix, A.; Neumann, B.; Stammler, H.-G.; Monkowius, U.; Gründlinger, P.; Mitzel, N. W. Hemi- and holodirected lead(ii) complexes in a soft ligand environment. *Dalton Trans.* **2015**, 44 (3), 924–937.
- (27) Rae, A. D.; Craig, D. C.; Dance, I. G.; Scudder, M. L.; Dean, P. A. W.; Kmetic, M. A.; Payne, N. C.; Vittal, J. J. The Pseudo-Symmetric Structure of Pb(SPh)₂. *Acta Crystallogr., Sect. B* **1997**, *53* (3), 457–465.
- (28) Gao, X.-S.; Dai, H.-J.; Ding, M.-J.; Pei, W.-B.; Ren, X.-M. Stereochemically Active and Inactive Lone Pairs in Two Room-Temperature Phosphorescence Coordination Polymers of Pb²⁺ with Different Tricarboxylic Acids. *Inorg. Chem.* **2019**, 58 (10), 6772–6780
- (29) Breza, M.; Bučinský, L.; Šoralová, S.; Biskupič, S. On the origin of the hemidirected geometry of tetracoordinated lead(II) compounds. *Chem. Phys.* **2010**, 368 (1), 14–19.

- (30) Shimoni-Livny, L.; Glusker, J. P.; Bock, C. W. Lone Pair Functionality in Divalent Lead Compounds. *Inorg. Chem.* **1998**, 37 (8), 1853–1867.
- (31) Coffey, A. H.; Yoo, P.; Kim, D. H.; Akriti; Zeller, M.; Avetian, S.; Huang, L.; Liao, P.; Dou, L. Structural Tunability and Diversity of Two-Dimensional Lead Halide Benzenethiolate. *Chem. Eur. J.* **2020**, 26 (29), 6599–6607.
- (32) Shaw, R. A.; Woods, M. Preparation and some properties of lead thiolates. J. Chem. Soc. A 1971, 0, 1569-1571.
- (33) Boudjouk, P.; Jarabek, B. R.; Simonson, D. L.; Seidler, D. J.; Grier, D. G.; McCarthy, G. J.; Keller, L. P. Metal Bis(benzylthiolates): Efficient Single Source Precursors to Solid Solutions and Nanoparticles of Metal Sulfides. *Chem. Mater.* **1998**, *10* (9), 2358–2364.
- (34) Robinson, K.; Gibbs, G. V.; Ribbe, P. H. Quadratic Elongation: A Quantitative Measure of Distortion in Coordination Polyhedra. *Science* **1971**, *172* (3983), 567–570.
- (35) Becke, A. D.; Edgecombe, K. E. A simple measure of electron localization in atomic and molecular systems. *J. Chem. Phys.* **1990**, 92 (9), 5397–5403.
- (36) Yakunin, S.; Chaaban, J.; Benin, B. M.; Cherniukh, I.; Bernasconi, C.; Landuyt, A.; Shynkarenko, Y.; Bolat, S.; Hofer, C.; Romanyuk, Y. E.; et al. Radiative lifetime-encoded unicolour security tags using perovskite nanocrystals. *Nat. Commun.* **2021**, *12* (1), 981.
- (37) Stadler, W.; Hofmann, D. M.; Alt, H. C.; Muschik, T.; Meyer, B. K.; Weigel, E.; Müller-Vogt, G.; Salk, M.; Rupp, E.; Benz, K. W. Optical investigations of defects in Cd_{1-x}Zn_xTe. *Phys. Rev. B* **1995**, *S1* (16), 10619–10630.
- (38) McCall, K. M.; Stoumpos, C. C.; Kostina, S. S.; Kanatzidis, M. G.; Wessels, B. W. Strong Electron–Phonon Coupling and Self-Trapped Excitons in the Defect Halide Perovskites $A_3M_2I_9$ (A = Cs, Rb; M = Bi, Sb). *Chem. Mater.* **2017**, 29 (9), 4129–4145.
- (39) Steele, J. A.; Puech, P.; Keshavarz, M.; Yang, R.; Banerjee, S.; Debroye, E.; Kim, C. W.; Yuan, H.; Heo, N. H.; Vanacken, J.; et al. Giant Electron—Phonon Coupling and Deep Conduction Band Resonance in Metal Halide Double Perovskite. *ACS Nano* **2018**, *12* (8), 8081–8090.
- (40) Smith, M. D.; Watson, B. L.; Dauskardt, R. H.; Karunadasa, H. I. Broadband Emission with a Massive Stokes Shift from Sulfonium Pb—Br Hybrids. *Chem. Mater.* **2017**, *29* (17), 7083–7087.
- (41) Benin, B. M.; Dirin, D. N.; Morad, V.; Wörle, M.; Yakunin, S.; Rainò, G.; Nazarenko, O.; Fischer, M.; Infante, I.; Kovalenko, M. V. Highly Emissive Self-Trapped Excitons in Fully Inorganic Zero-Dimensional Tin Halides. *Angew. Chem., Int. Ed.* **2018**, *57* (35), 11329–11333.
- (42) Zeng, R.; Zhang, L.; Xue, Y.; Ke, B.; Zhao, Z.; Huang, D.; Wei, Q.; Zhou, W.; Zou, B. Highly Efficient Blue Emission from Self-Trapped Excitons in Stable Sb³⁺-Doped Cs₂NaInCl₆ Double Perovskites. *J. Phys. Chem. Lett.* **2020**, *11* (6), 2053–2061.
- (43) Luo, J.; Wang, X.; Li, S.; Liu, J.; Guo, Y.; Niu, G.; Yao, L.; Fu, Y.; Gao, L.; Dong, Q.; et al. Efficient and Stable Emission of Warm-White Light from Lead-Free Halide Double Perovskites. *Nature* **2018**, 563 (7732), 541–545.
- (44) Dohner, E. R.; Jaffe, A.; Bradshaw, L. R.; Karunadasa, H. I. Intrinsic white-light emission from layered hybrid perovskites. *J. Am. Chem. Soc.* **2014**, *136* (38), 13154–13157.
- (45) Yang, H.; Cai, T.; Liu, E.; Hills-Kimball, K.; Gao, J.; Chen, O. Synthesis and Transformation of Zero-Dimensional Cs_3BiX_6 (X = Cl, Br) Perovskite-Analogue Nanocrystals. *Nano Res.* **2020**, *13* (1), 282–291.
- (46) Liu, Z.; Sun, Y.; Cai, T.; Yang, H.; Zhao, J.; Yin, T.; Hao, C.; Chen, M.; Shi, W.; Li, X.; et al. Two-Dimensional Cs₂AgIn_xBi_{1-x}Cl₆ Alloyed Double Perovskite Nanoplatelets for Solution-Processed Light-Emitting Diodes. *Adv. Mater.* **2023**, *35* (19), 2211235.
- (47) Smith, M. D.; Connor, B. A.; Karunadasa, H. I. Tuning the Luminescence of Layered Halide Perovskites. *Chem. Rev.* **2019**, *119* (5), 3104–3139.
- (48) Lee, W. S.; Cho, Y.; Powers, E. R.; Paritmongkol, W.; Sakurada, T.; Kulik, H. J.; Tisdale, W. A. Light Emission in 2D Silver Phenylchalcogenolates. *ACS Nano* **2022**, *16* (12), 20318–20328.

- (49) Giannozzi, P.; Baroni, S.; Bonini, N.; Calandra, M.; Car, R.; Cavazzoni, C.; Ceresoli, D.; Chiarotti, G. L.; Cococcioni, M.; Dabo, I.; et al. QUANTUM ESPRESSO: a modular and open-source software project for quantum simulations of materials. *J. Phys.: Condens. Matter* **2009**, *21* (39), No. 395502.
- (50) Perdew, J. P.; Burke, K.; Ernzerhof, M. Generalized gradient approximation made simple. *Phys. Rev. Lett.* **1996**, 77 (18), 3865.
- (51) Kresse, G.; Joubert, D. From ultrasoft pseudopotentials to the projector augmented-wave method. *Phys. Rev. B* **1999**, 59 (3), 1758–1775.
- (52) Grimme, S.; Antony, J.; Ehrlich, S.; Krieg, H. A consistent and accurate ab initio parametrization of density functional dispersion correction (DFT-D) for the 94 elements H-Pu. *J. Chem. Phys.* **2010**, 132 (15), 154104.
- (53) Heyd, J.; Scuseria, G. E.; Ernzerhof, M. Hybrid functionals based on a screened Coulomb potential. *J. Chem. Phys.* **2003**, *118* (18), 8207–8215.